Radio-Frequency Vector Magnetic Field Mapping in Magnetic Resonance Imaging

Seung-Kyun Lee, *Member, IEEE*, Sukhoon Oh, Hyeong-Seop Kim,
and Byung-Pan Song

Abstract—A method is presented to measure the radio-frequency (RF) vector magnetic field inside an object using magnetic resonance imaging (MRI). Conventional "B_1 mapping" in MRI can measure the proton co-rotating component (B_1^+) of the RF field produced by a transmit coil. Here we show that by repeating B_1^+ mapping on the same object and coil at multiple (8) specific orientations with respect to the main magnet, the magnitudes and relative phases of all (x, y, z) Cartesian components of the RF field can be determined unambiguously. We demonstrate the method on a circularly polarized volume coil and a loop coil tuned at 123.25 MHz in a 3 Tesla MRI scanner, with liquid phantoms. The volume coil measurement showed the axial component of the RF field, which is normally unmeasurable in MRI, away from the center of the coil. The measured RF vector field maps of both coils compared favorably with numerical simulation, with volumetric normalized root-mean-square difference in the range of 7~20%. While the proposed method cannot be applied to human imaging at present, applications to phantoms and small animals could provide a useful experimental tool to validate RF simulation and verify certain assumptions in B_1^+ map-based electrical properties tomography (EPT).

Index Terms—B1 map, magnetic resonance imaging (MRI), multi-orientation imaging, radio-frequency (RF) field.

I. Introduction

IN MAGNETIC resonance imaging (MRI), a pulsed radio-frequency (RF) magnetic field (B_1) induces the ^{1}H (proton) spin excitation and thereby initiates the imaging sequence. The B_1 field also performs inversion, saturation, refocusing, and spoiling of the proton magnetization. In high static-field (B_0) MRI, say at 3T and above, the RF wavelength inside the biological tissue becomes comparable to the size of the human body, which results in significant image shading and contrast variation [1]. Solutions to mitigate this problem, such as B_1 shimming and parallel transmit, require measurement of the shaded RF fields from the transmit coils, and a variety of B_1 mapping methods have been developed for this purpose over the years [2,3]. Importantly, since the proton spins only interact with the proton co-rotating component of the RF field in the transverse plane (defined by B_0), B_1 mapping needs to, and in fact is able to, address only such a component, which is called B_1^+. In what follows we will distinguish between B_1, a general term for an RF magnetic field with 3 components, and B_1^+, which is its component measurable by conventional B_1^+ mapping. We further note that the latter measures only the magnitude of B_1^+; we will therefore use B_1^+ mapping and $|B_1^+|$ mapping interchangeably.

A closely related problem in high-field MRI is RF-induced tissue heating, commonly defined by the specific absorption rate (SAR). This has to be modeled during design and monitored during operation of an RF transmit coil to ensure patient safety. While the whole-body (global) energy transfer to the subject can be reasonably well tracked by the transmitted power at the coils, local tissue heating cannot easily be measured non-invasively. Numerical simulation, therefore, plays a central role in predicting the RF heating power, $P = \int \sigma E^2 dv$, where σ is the tissue conductivity and E is the rms electric field magnitude. Unlike in RF shading, experimental B_1^+ mapping is insufficient to replace simulation because all three components of B_1 contribute to the induced electric field and thereby heating. Several authors have proposed methods to estimate SAR from the measured B_1^+ maps [4]–[8]. They generally rely on the fact that RF transmit coils often produce dominant transverse B_1 fields, possibly allowing one to ignore B_{1z} that is not measurable in MRI. While encouraging results have been reported, omission of B_{1z} in cases involving highly localized transmit coils or strong RF perturbing sources is

still questionable. In current RF safety practices, therefore, B_1^+ mapping plays a relatively limited role of validating the simulation software itself [9] through B_1^+ maps in phantoms.

Calculating "power (P)" through simulation also requires knowledge of the electrical properties (σ and relative permittivity, ϵ_r) of the tissue. While tabulated values are usually substituted for them, *in vivo* measurement of these parameters from B_1^+ mapping has been proposed [8], [10], [11]. Among a host of such methods, collectively called MR-based electrical properties tomography (MREPT), many recent proposals theoretically require the axial (B_{1z}) as well as the transverse components of the RF field to reduce artifacts [12]–[14]. As in the SAR calculation, the unmeasurable, B_{1z} component is usually ignored by resorting to coil geometry arguments.

Currently, there is no direct way to measure the RF field components other than B_1^+ using MRI. Our work is motivated by the realization that if the RF coil and the medium (together, "RF system") are to be reoriented in the MRI magnet, the components of the RF fields are re-defined, and thereby can make previously unmeasurable components experimentally accessible [15]–[17]. Specifically, from the RF system's point of view, the axial component B_{1z} is arbitrarily assigned according to the direction of B_0. As B_0 reorients relative to the RF system, the same RF component will now be projected on the (new) transverse plane, and picked up by B_1^+ mapping.

In our opinion, the ability to measure all three components of the RF magnetic field is useful in the following respects: First, simulation validation can be more complete. This will especially be true if a large portion of the RF energy resides in non-B_1^+ components, which can be caused by e.g., metallic objects [18] in an otherwise B_1^+-dominant transmit coil. Second, the ability to measure B_{1z} can help verify certain assumptions in MREPT methodologies as mentioned above. Lastly, there may be circumstances when RF simulation is difficult, for example when the coil configuration is not known for proprietary reasons, or when engineered or biological materials with unknown electrical properties are included in the system under investigation [19]. In such cases, experimental field mapping may be the only way to find the RF energy distribution in the system.

In all the examples above, RF vector field measurements will be helpful and relevant even if such measurements can only be done in phantoms or small animals. Human subject application will be extremely valuable, but the lack of it does not preclude other useful applications.

The idea of multi-orientation B_1^+ mapping for RF vector field measurement was sketched as early as in 1995 [15] as a means for RF current density imaging [20] with externally injected RF current. Application of the method in the context of high-field RF shading and MREPT was proposed in [16] in 2006, but to our knowledge was not experimentally pursued. A related idea of turning an object by 180° to map the counter-rotating component (B_1^-) has been demonstrated experimentally [21]. In this paper, we present a specific experimental design, following the general idea of [16], that consists of B_1^+ mappings on an object with a rigidly attached RF coil in 8 different orientations in the magnet. The method produces the magnitudes and relative phases of the three Cartesian
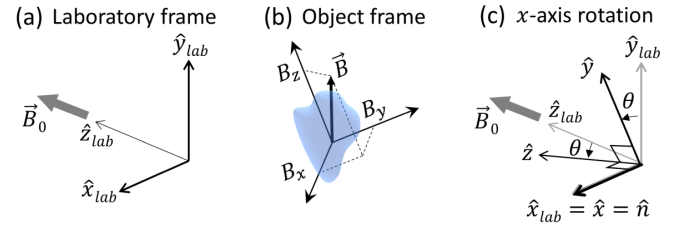

Fig. 1. (a-b) Frames of reference to define the laboratory- and object-frame coordinates of the RF magnetic field $\vec{B}$. (c) Example of object frame rotation around the *x*-axis ($\hat{n}=\hat{x}=\hat{x}_{lab}$) by θ.

components of the RF vector field in the object's frame of reference. The absolute RF phase is not obtainable by any number of measurements of only the B_1^+ magnitudes. However, we show that the relative phases among different components are nonetheless calculable, through mixing of these components following rotation of the coordinate system. We emphasize that our method does not require any phase imaging.

Below, we first explain the theory of RF vector magnetic field measurement. Then we describe experimental realizations of the proposed method on a cylindrical volume coil and a loop coil with liquid phantoms. The measured RF components are then compared with the results from RF simulation.

II. THEORY

A. Problem Definition

Consider an RF transmit coil and an MR-visible object that are fixed relative to each other. This assembly is referred to as an "RF system". The laboratory coordinate system ($x_{lab}, y_{lab}, z_{lab}$) is defined such that z_{lab} is along the main magnetic field (Fig. 1). In the transverse plane, $\hat{y}_{lab}$ is (arbitrarily) defined along the vertical direction, and $\hat{x}_{lab} \equiv \hat{y}_{lab} \times \hat{z}_{lab}$. Here $^\wedge$ denotes the unit vector. The RF system has its own coordinates (x, y, z) defined on a reference frame fixed to the object. Our goal is to find the magnitudes and relative phases of all three components of the RF fields (B_x, B_y, B_z) in the object's frame of reference, inside the object. For notational simplicity, here and in what follows, we reserve the notation B or $\vec{B}$ without subscript "1" for the RF magnetic field, when it does not cause confusion with B_0. Since we assume that B_0 is in the positive z_{lab} direction, the ^{1}H spins precess in the negative (clockwise) direction in the transverse plane. What is measured in conventional B_1^+ mapping is then the magnitude of the circularly polarized component of the RF field, defined as $B_{lab}^+ \equiv (B_{x,lab} - i B_{y,lab})/2$ in the laboratory frame; its relationship with the object-frame RF components depends on the RF system's orientation (Fig. 1).

B. Relationship Between B_{lab}^+ and (B_x, B_y, B_z)

Suppose first that the object frame coincides with the laboratory frame. The component B_{lab}^+ is then simply

$$B_{lab}^+ = (B_x - i B_y)/2. \tag{1}$$

In order to proceed, we make an important but realistic assumption that the RF field vector is "frozen" in the object's

frame of reference, regardless of its orientation. In particular, we assume that the RF field to be measured is sufficiently localized that it is not affected by, e.g., the RF shield fixed on the magnet or any other structure that is fixed in the laboratory. In practice, this requires an RF coil that is small compared to the bore of the magnet. Alternatively, the RF coil and the object could be in a separate RF shield for their isolation from the environment. In such a case our "RF system" should include the shield.

Now suppose that the object (more precisely, RF system) is rotated by an angle θ around a unit vector $\hat{n}$ defined in the laboratory frame (Fig. 1c). The three components of $\vec{B} = (B_x, B_y, B_z)$ in the object frame do not change. But their projections on the laboratory coordinate axes, $\vec{B}_{lab} = (B_{x,lab}, B_{y,lab}, B_{z,lab})$, will change, according to

$$\vec{B}_{lab} = \mathbf{R}\vec{B}$$
$$= \hat{n}\left(\hat{n} \cdot \vec{B}\right) + \cos\theta\left(\vec{B} - \hat{n}\left(\hat{n} \cdot \vec{B}\right)\right) + \sin\theta\left(\hat{n} \times \vec{B}\right). \quad (2)$$

where $\mathbf{R}$ is the 3D rotation matrix [22]. From this, the magnitude of B_{lab}^+ which is experimentally measured becomes

$$\left|B_{lab}^+\right| = \left|B_{x,lab} - iB_{y,lab}\right|/2$$
$$= \frac{1}{2}|\left(\cos\theta - in_z\sin\theta\right)\left(B_x - iB_y\right) + B_z\left(n_y + in_x\right)$$
$$\times \sin\theta + \vec{B} \cdot \hat{n}(n_x - in_y)(1 - \cos\theta)|. \quad (3)$$

Therefore the three RF components in the object frame enter into $\left|B_{lab}^+\right|$ in a complicated manner. Obviously, a single measurement of $\left|B_{lab}^+\right|$ will not suffice for their determination. Our goal is to devise a set of rotations $\hat{n}, \theta$ that will produce enough number of equations like Eq. (3) to be solved for the five unknowns: magnitudes of (B_x, B_y, B_z), and their relative phases.

C. Eight-Orientation Solution

Since Eq. (3) is nonlinear, five unknowns may well require more than five equations for their unambiguous determination. Among many possibilities, in this work we highlight one particular set of eight rotations that are capable of producing measurement data that can be converted to the following eight real quantities: $|B_x|$, $|B_y|$, $|B_z|$, $Re\left(B_x B_y^*\right)$, $Im\left(B_x B_y^*\right)$, $Im\left(B_y B_z^*\right)$, $Re\left(B_z B_x^*\right)$, $Im\left(B_z B_x^*\right)$. The relative phase between B_x and B_y can be determined by the real and imaginary parts of $B_x B_y^*$, and the phase between B_z and B_x can likewise be determined by the real and imaginary parts of $B_z B_x^*$. Since these uniquely determine the 3rd relative phase, $\angle\left(B_y B_z^*\right)$, the quantity $Im\left(B_y B_z^*\right)$ is redundant given that $|B_y|$ and $|B_z|$ are already available. As we will see, however, this redundancy helps determine $\angle\left(B_y B_z^*\right)$ when B_x is small.

Table I lists the eight rotations along with the quantities measured through B_1^+ mapping at each orientation. The rotations are expressed as the rotation axis (in the laboratory frame, omitting subscript "lab") followed by the angle in degrees, as in "y90" for rotation by 90 degrees around the

TABLE I
EIGHT ORIENTATIONS AND MEASURED QUANTITIES

Orientation (axis, angle)	Measured quantities ($= \left\|B_{lab}^+\right\|$)
y0	$M_1 \equiv \left\|B_x - iB_y\right\|/2$
y45	$M_2 \equiv \left\|(B_x + B_z)/\sqrt{2} - iB_y\right\|/2$
y90	$M_3 \equiv \left\|B_z - iB_y\right\|/2$
y180	$M_4 \equiv \left\|B_x + iB_y\right\|/2$
y270	$M_5 \equiv \left\|B_z + iB_y\right\|/2$
x90	$M_6 \equiv \left\|B_x + iB_z\right\|/2$
x90 then y45	$M_7 \equiv \left\|(B_x + B_y)/\sqrt{2} + iB_z\right\|/2$
x90 then y180	$M_8 \equiv \left\|B_x - iB_z\right\|/2$

TABLE II
FORMULAS FOR THE PRODUCTS OF RF FIELD COMPONENTS

Output	Expression
$\|B_x\|^2$	$M_1^2 - M_3^2 + M_4^2 - M_5^2 + M_6^2 + M_8^2$
$\|B_y\|^2$	$M_1^2 + M_3^2 + M_4^2 + M_5^2 - M_6^2 - M_8^2$
$\|B_z\|^2$	$-M_1^2 + M_3^2 - M_4^2 + M_5^2 + M_6^2 + M_8^2$
$Re(B_x B_y^*)$	$\left(-1 - \sqrt{2}\right)(M_3^2 + M_6^2) - \left(1 - \sqrt{2}\right)(M_5^2 + M_8^2)$ $+ 4M_7^2$
$Im(B_x B_y^*)$	$M_4^2 - M_1^2$
$Im(B_y B_z^*)$	$M_3^2 - M_5^2$
$Re(B_z B_x^*)$	$\left(-1 - \sqrt{2}\right)(M_1^2 + M_3^2) - \left(1 - \sqrt{2}\right)(M_4^2 + M_5^2)$ $+ 4M_2^2$
$Im(B_z B_x^*)$	$M_8^2 - M_6^2$

laboratory's y axis. Table II summarizes the formulas for the eight output quantities that are calculated from the measurements in Table I. The derivations of these formulas are available in Supplementary materials, section 1.

It is acknowledged that the above eight-orientation solution is one of many possible solutions for the proposed vector RF mapping. In particular, it departs from the six-orientation suggestion in [16]. The current solution was devised with two desirable features in mind: (i) The data should be sufficient to calculate $\vec{B}_1$ components deterministically with as little assumption as possible. The formulas in Table II involve only straightforward arithmetic operations on the measured data. (ii) The rotation axis is predominantly $\hat{y}$ (vertical) in the laboratory frame, and rotation around the other axes is minimized. This facilitates experiments on liquid phantoms and potentially small animals.

III. METHODS

Two experiments were performed to demonstrate our method: one with a commercial knee imaging coil with separate transmit (circularly polarized volume coil) and receive (multi-channel array) elements, and the other with a home-made single-channel loop coil for both transmission and reception. All MRI scans were performed with a human whole-body 3T scanner (Magnetom Prisma, Siemens, Erlangen, Germany) with the center frequency $f_0 = 123.25$ MHz.
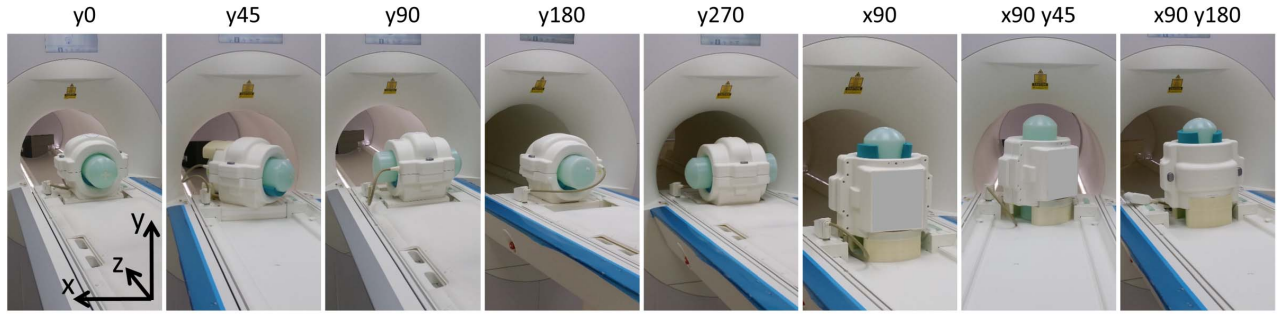
Fig. 2. Pictures of a knee coil and a cylindrical phantom that were set up at eight different orientations per Table I. At each orientation, the coil and the phantom maintained their relative positions.

A. Volume Coil Setup

The knee coil (Siemens) consisted of a circularly polarized volume transmission coil and a 15-element receiver array. We scanned a vendor-provided liquid cylindrical phantom (Model 10606530 K2305), containing an aqueous solution of 3.75 g/L $NiSO_4(H_2O)_6$ and 5 g/L NaCl, and measuring 42 cm (length) × 14.5 cm (diameter).

The phantom was radially centered and firmly held in the coil by foam pads. The phantom and the coil comprised our "RF system" to be rotated together as one body. Figure 2 illustrates the eight orientations of the phantom according to Table I, as the phantom and the coil were set up on the patient table before being inserted in the magnet bore. The coordinate axes shown on the image for the default orientation (y0) correspond to the object frame coordinates that are fixed to the phantom; these axes move along with the phantom. Our goal is to find the RF magnetic field components along these axes in the phantom, produced by the transmit coil. In the default orientation, the object frame coincides with the laboratory frame. The first 5 orientations were easily realized, only constrained by the length of the RF cable. For the last 3 orientations the RF coil had to stand upright. A pair of 3D-printed plastic pieces supported the coil in these positions (Fig. 2, last three images).

B. Loop Coil Setup

A home-made circular loop coil with inner/outer diameter of 9.7 cm/10.3 cm was tuned to f_0 and interfaced with the scanner's RF transmit and receive system. The phantom consisted of three glass bottles each with diameter/length of 3 cm/9 cm. The bottles were filled with physiological saline (9 g/L NaCl in water), half-density saline (4.5 g/L NaCl in water), and canola oil. The two saline solutions were also doped with 1 mM of Gd-based contrast agent (Dotarem, Guerbet, Villepinte, France) to reduce the longitudinal relaxation time (T_1). T_1 was measured by applying the steady-state signal equation to 90°-flipped spoiled gradient echo images at 7 different repetition times in a separate experiment. The measured T_1 values for the saline, half saline, and oil were 143 ms, 154 ms, and 220 ms, respectively. The bottles were rigidly held by insertion into three tight-fitting holes in a 3D-printed plastic frame, arranged in an equilateral triangle with center-to-center distance of 4 cm. The plastic frame was a rectangular block measuring 10 cm × 10 cm × 8 cm (height).

Our "RF system" consisted of the loop coil and the glass bottles in the plastic block.

In order to reliably implement the orientations prescribed in Table I, while ensuring that the RF field from the coil has sufficient components perpendicular to B_0, we devised a two-piece support hardware where the phantom could be placed slanted by 45° (Fig. 3 and Supplementary materials, section 2). The first piece was an M-shaped acrylic block whose "V" received the phantom. This piece had a bottom that could snugly fit into a 2 cm-high acrylic baseplate that was taped on the patient table. The baseplate had a 1 cm-deep octagonal depression pattern so the M-shaped block could be seated in different orientations at 45° increments. Figure 3 shows the eight final orientations of the phantom. As in Fig. 2, the coordinate axes shown in the default orientation (y0) define the object frame coordinates that moved with the phantom. In our design the cylindrical axes of the bottles and the loop coil were always at 45° with respect to the vertical axis. This ensured that air bubbles remained at the top of the bottles, and the RF field maintained a component normal to B_0.

C. B_1^+ Mapping

For both experiments, at each phantom orientation the circularly polarized component $|B_{lab}^+|$ of the RF field in the laboratory frame was measured by B_1^+ mapping. We used two different methods for the two coils because the dynamic range of $|B_{lab}^+|$ was much different. For the volume coil, we used the scanner-provided sequence of saturation-prepared fast gradient echo (GRE) imaging [23]. This was fast but insufficient to cover the wide range of $|B_{lab}^+|$ encountered in the loop coil experiment. For the latter, therefore, we used a slow but straightforward method where the GRE magnitudes at four different transmitter voltages were fitted to a sine curve to determine the flip angle per voltage (β), in [°/V].

1) Volume Coil Experiment: The experimental procedures are listed below.

Step 1. Set up the coil and the phantom in the default (y0) orientation.

Step 2. Perform a localizer scan.

Step 3. Scan for B_1 mapping in the axial plane in the object's reference frame; that is, perpendicular to the phantom's cylindrical axis. For the y0 orientation this is the same as the conventional axial plane. Make sure that the transmit voltage is kept constant (reference voltage, V_r) when scanning
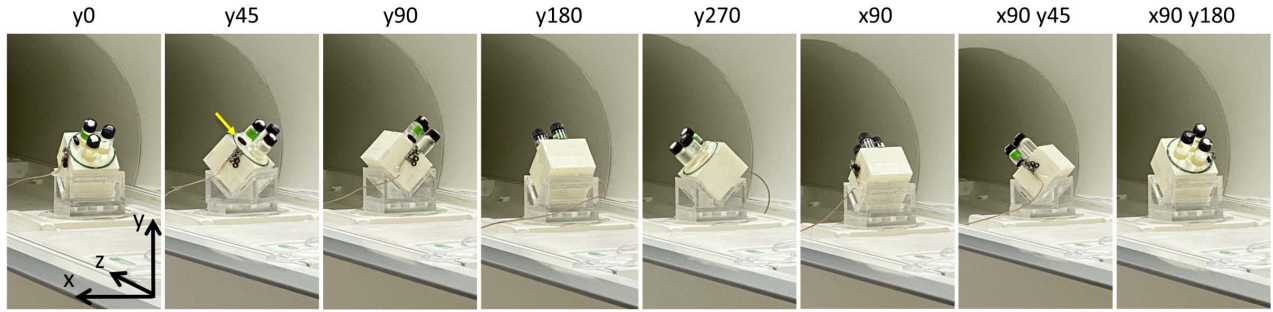
Fig. 3. Pictures of a loop coil and a three-bottle phantom that were set up at the eight orientations of Table I. At each orientation, the coil and the phantom maintained their relative positions and moved as one body. Clear, acrylic M-shaped block supported the phantom at 45°. A vitamin pill (yellow arrow) was glued to the phantom for easy identification of the bottles in MR images.

at different orientations. Otherwise the scanner tends to impose a predetermined average flip angle by automatically adjusting the voltage based on a scout scan, which makes comparison of B_1 maps at different orientations difficult. In our experiment, a fixed transmit voltage of 161 V was manually entered into the scan prescription window. The scan parameters were: TR = 9000 ms, TE = 1.7 ms, flip angle = 8°, pixel bandwidth = 490 Hz/px, pixel size = 1.17 mm × 1.17 mm, matrix size = 128 × 128, field of view (FOV) = 150 mm × 150 mm, slice thickness = 8 mm, slice spacing (center-to-center) = 16 mm, number of slices = 18, averages = 1, acquisition type = 2D, scan time = 48 s.

Step 4. Set up the coil and the phantom for the next orientation. Repeat at Steps 2 until all orientations are covered. The scan plane for B_1 mapping was always perpendicular to the axis of the phantom.

2) Loop Coil Experiment: The experimental procedures are similar to the above.

Step 1. Set up the loop coil and the phantom in the default (y0) orientation.

Step 2. Perform a localizer scan.

Step 3. Scan the phantom with a GRE sequence. The scan is prescribed in the "yz" plane in the object's reference frame; this is the plane that contains the "M" of the M-shaped block. In the y0 orientation this corresponds to the conventional sagittal plane. The scan parameters were: TR = 1380 ms, TE = 4.9 ms, pixel bandwidth = 1185 Hz/px, pixel size = 1.17 mm × 1.17 mm, matrix size = 96 × 128, field of view (FOV) = 112.5 mm × 150 mm, slice thickness = 1.5 mm, no slice gap, number of slices = 64, averages = 1, acquisition type = 2D, scan time = 1 min 54 s. The scan was repeated with 4 different transmit voltages V that were manually set: 16 V, 32 V, 64 V, 128 V.

Step 4. Set up the coil and the phantom for the next orientation. Repeat at Steps 2 until all orientations are covered. At each orientation the scan plane was prescribed parallel to the side wall of the M-shaped block; in the laboratory frame this was either sagittal, axial, or half-way (45°) between them.

D. Data Processing

For the volume coil scan, the B_1^+ maps in terms of the flip angle at the reference voltage were automatically generated after each scan. The B_1^+ maps at different orientations were then registered off-line to the default-orientation map, and the equations in Table II were applied to compute the object-frame B_1 components. All data processing was done in MATLAB (Mathworks, Natick, MA, USA).

For the loop coil experiment, the flip angle per voltage (β) was obtained by fitting the image magnitudes (S) as a function of V to a sine function: $S = S_0 \sin(\beta V \times \pi/180)$. Masking was applied to reject voxels where the GRE signal was too low (thresholded at 5% of maximum), or the fitting residual was too large (rms residual being greater than 10% of the maximum signal). As with the volume coil data, all the flip angle maps were registered to the y0 orientation, and Table II was used to compute the object-frame B_1 components.

For quantitative comparison between the measured and simulated B_1 component maps, both maps were resampled on the same grid consisting of 9 slices normal to the cylindrical axes of the phantom. The simulated maps were geometrically aligned with the measured maps on each slice and normalized to match the volume rms of $|\vec{B}_1|$ of the measured data.

E. Simulation

For both experiments, the RF fields from the respective coil model were simulated in XFdtd 7.7 (Remcom, State College, PA, USA), on a 64 bit PC with 128 GB RAM and AMD 3700x CPU equipped with an NVIDIA 1080 GPU.

1) Volume Coil Simulation: We used proprietary coil parameters provided by Siemens for the volume coil simulation. The cylindrical phantom was given electrical properties $\sigma = 1$ S/m and $\epsilon_r = 78$. The coil was simulated at 123.25 MHz with current sources driving a circularly polarized RF field. All three complex components of the RF field in the phantom were simulated and collected at the steady state of the magnetic field propagation. The cell and mesh sizes were $2 \times 2 \times 2$ mm^3 and $420 \times 417 \times 870$, respectively. The simulation took about 38 minutes.

2) Loop Coil Simulation: The loop coil was modeled as an annular ring with the same dimensions as the actual coil. Four constant current sources were placed at the locations of the tuning capacitors, and simulated at 123.25 MHz to compute the complex RF field components. The bottles for the saline, half-density saline, and oil were modeled with the electrical properties $(\sigma, \epsilon_r) = (1.7$ S/m, 78), (0.86 S/m, 78), (0.07 S/m, 12), respectively. 1-mm isotropic cells in a mesh of size $222 \times 170 \times 222$ were used. The simulation took about 3 minutes.
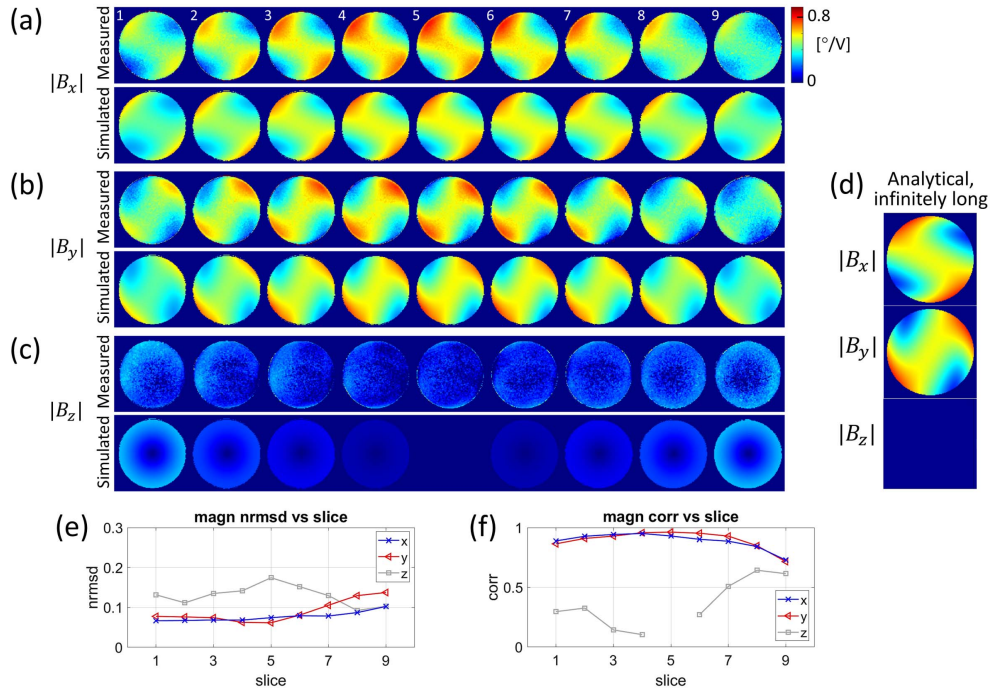
Fig. 4.　(a-c) Measured vs simulated $\vec{B}_1$ components on nine consecutive slices of a cylindrical phantom. The 5th slice corresponds to the middle of the phantom. Measured data are displayed in unit of flip angle (°) per volt. Simulated data were normalized by a single scaling factor to match the rms $|\vec{B}_1|$ of the measured data. (d) Analytical results for an infinitely long cylinder in a uniform, circularly polarized RF field, in arbitrary unit, to be compared with the 5th slice in (a-c). (e) Root-mean-square difference between the measured and simulated B_1 components on each slice, normalized by the volume rms of $|\vec{B}_1|$. (f) Pearson correlation coefficients for the B_1 components on all slices (except the 5th slice for B_z).

IV. RESULTS

A. Volume Coil RF Vector Field

Fig. 4(a-c) shows the magnitudes of the volume coil's RF field components that were calculated from the eight-orientation B_1^+ mapping data, compared with simulation. We observe that $|B_x|$ and $|B_y|$ are each strongly inhomogeneous, and are approximately 90° rotated versions of each other. In comparison, $|B_z|$ is more symmetric and relatively weak. We emphasize that conventional B_1^+ mapping cannot distinguish the Cartesian components of an RF field in this manner. In particular, the z component of the RF field is normally not measurable. Our result shows that $|B_z|$ is very small in the center slice, but grows noticeably in magnitude away from the center.

This is an expected behavior of a finite-length volume coil, and is confirmed by the simulation. Fig. 4(d) shows analytically calculated RF field components inside an infinitely long cylinder in a circularly polarized RF driving field [24]. The three components match closely the measured and simulated data in the central slice (slice 5), where the RF field is expected to be the least affected by the finite length of the coil.

For quantitative comparison, the rms differences and the Pearson correlation coefficients between the measured and simulated B_1 components were calculated per slice (Fig. 4(e-f)). The rms difference was normalized by the measured volume rms of $|\vec{B}_1|$ (=0.70°/V), which was also used to scale the simulated data. Both the differences and the correlations were the worst for B_z, which was the weakest of the three components and potentially the most sensitive to

experimental imperfections (such as misalignment of phantom and coil). The slice-averaged normalized rms difference was 7.7%, 8.9%, and 13.0% for $|B_x|$, $|B_y|$, and $|B_z|$, respectively.

The relative phase angles between the RF field components are shown in Fig. 5(a-c). There was no adjustable parameter in displaying these results. The phase $\angle B_x - \angle B_y$ shows that on the average B_x is lagging (having more negative phase than) B_y by about 90°, as expected for a left circularly polarized field producing B_1^+. This phase difference is not uniform within and across the slices. The measured spatial patterns of $\angle B_x - \angle B_y$ showed good qualitative agreement with the simulation (Fig. 5(a)) as well as the analytical result (Fig. 5(d)). We note that because of the weak B_z magnitude, measured phases involving B_z are less reliable; they are more susceptible to noise and systematic errors. In theory, $\angle B_z$ is not even defined on the central slice where $B_z = 0$. To account for magnitude-dependent phase uncertainty, we also calculated the rms difference in the complex products $B_x B_y^*$, $B_y B_z^*$, $B_z B_x^*$, which represent magnitude-weighted complex phase factors (Fig. 5(f)). When normalized by the volume-averaged $|\vec{B}_1|^2$, the measurement-simulation difference was below about 12%. Fig. 5(g) shows the correlation coefficients for the same complex products. As one moves away from the center towards the end slices, the measured $B_y B_z^*$, $B_z B_x^*$ maps showed higher correlation (>0.6) with the simulation.

B. Loop Coil RF Vector Field

Fig. 6(a-c) compares the measured and simulated RF field components of the loop coil. The simulated maps were scaled
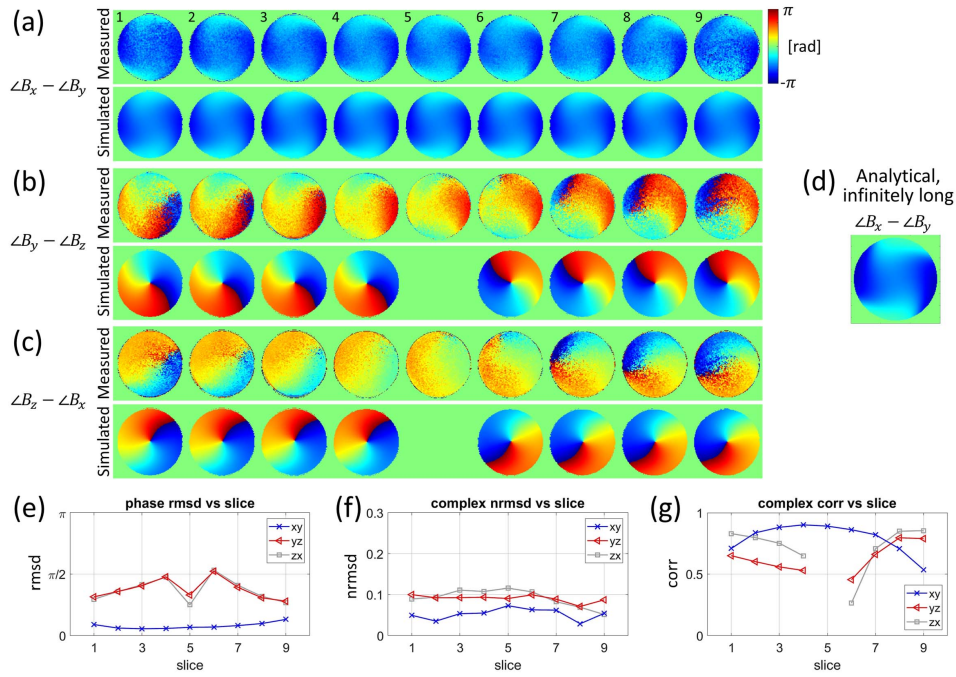
Fig. 5. (a-c) Measured vs simulated relative phase maps between the $\vec{B}_1$ components in the same phantom as in Fig. 4. (d) Analytical relative phase between the transverse components for an infinitely long cylinder, to be compared with the 5th slice in (a). (e) Root-mean-square difference between the measured and simulated phases on each slice (calculated in the complex plane). (f-g) Magnitudes of the normalized rms difference (f) and the Pearson correlation coefficients (g) between the "measured and simulated" complex products ($B_x B_y^*$, $B_y B_z^*$, $B_z B_x^*$) on all slices (except the 5th slice for B_z). The normalization in (f) was by the volume-averaged $\left|\vec{B}_1\right|^2$.
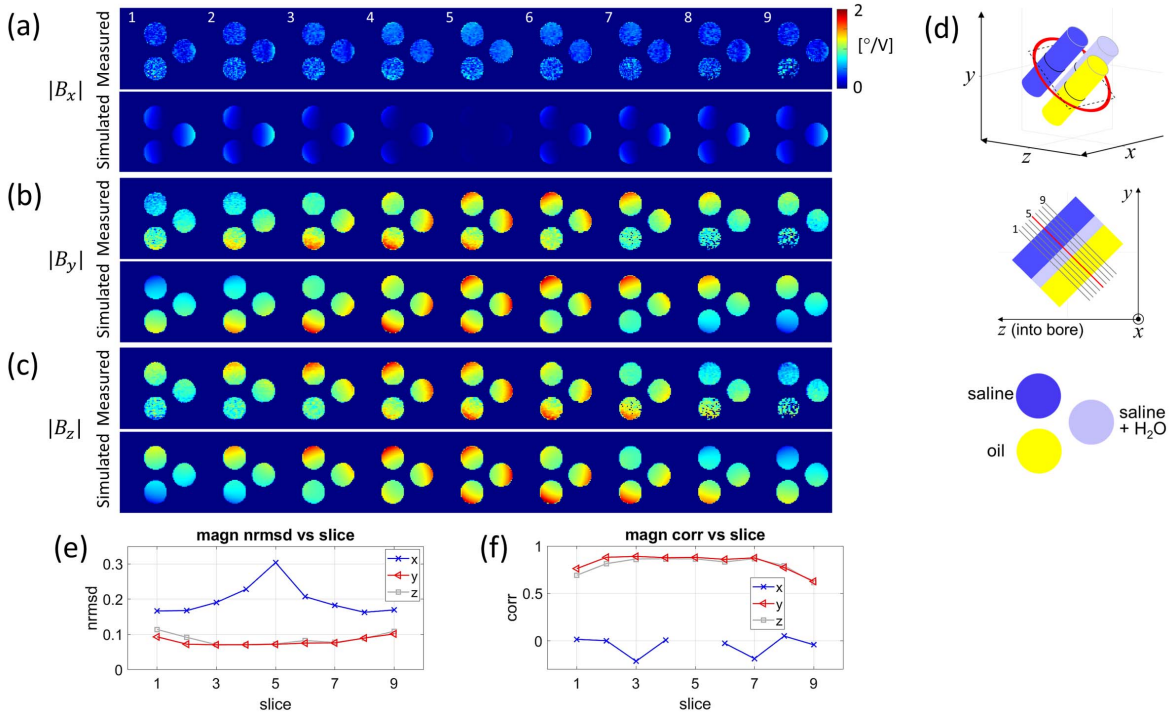

Fig. 6. (a-c) Measured vs simulated $\vec{B}_1$ components in the three-bottle phantom. Nine consecutive slices perpendicular to the bottles' long axes are shown, as sketched in (d) in the default (y0) orientation. Measured data are displayed in unit of flip angle (°) per volt. Simulated data were normalized by a single scaling factor to match the rms $|\vec{B}_1|$ of the measured data. (e) Root-mean-square difference between the measured and simulated B_1 components on each slice, normalized by the volume rms of $\left|\vec{B}_1\right|$. (f) Pearson correlation coefficients for the B_1 components.

to match the rms $\left|\vec{B}_1\right|$ of the measured data (1.52°/V). In our setup (Fig. 6(d)), the loop coil's RF field is supposed to project equally onto the y and z axes on the central slice (slice 5), whereas $|B_x|$ should be zero on the slice and remain weak throughout the phantom. There is good visual agreement between the measured and simulated $|B_y|$ and
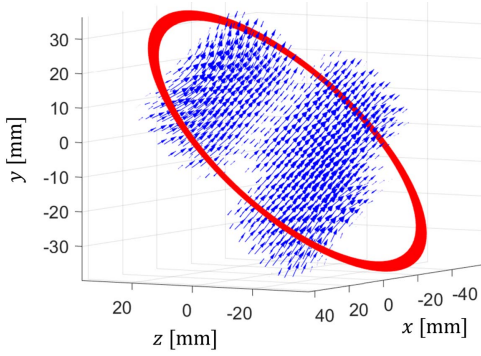
Fig. 7. Arrow plot of the measured RF vector field from the loop coil (red). The middle section of the phantom that corresponds to the slices of Fig. 6 is shown. The arrows correspond to the RF magnetic field when the phase of the y component is zero.

$|B_z|$ maps. The measured $|B_x|$ maps, on the other hand, did not fully capture the vanishing magnitudes on the central slice and along the vertical midlines on all other slices. The normalized rms difference and the correlation coefficient plots (Fig. 6(e-f)) confirm this observation. In particular, the slice-averaged rms difference in $|B_x|$ was 19.8% of the norm ($=$ rms $|\vec{B}_1|$), much higher than those for $|B_y|$ (8.0%) and $|B_z|$ (8.7%). This discrepancy is not fully understood and needs to be further investigated. The observed spatial distribution of the RF fields is mostly determined by the coil's geometry rather than the phantom's electrical properties. We did not observe significant difference among different liquid materials in the phantom (see slice 5). This was confirmed by another simulation (not shown) where we intentionally changed the order of the liquid materials; swapping oil and half-saline resulted in less than 3% change in the RF field magnitudes. Fig. 7 shows 3D rendering of the RF field vectors from the measured data. A 360° rotating view is available as an animation file in Supplementary materials. The field lines are oriented approximately normal to the coil's plane, while being slightly bent around the coil's ring.

Fig. 8(a-c) shows the measured relative phase maps in comparison with simulation. Because $|B_x|$ is small the phase difference involving $\angle B_x$ is expected to be noisy. For the measurement, we first calculated $\angle B_y - \angle B_z$ from the knowledge of $Im\left(B_y B_z^*\right)$ and $|B_y|$, $|B_z|$ (see Appendix for details). Then we calculated $\angle B_x - \angle B_y$ from the real and imaginary parts of $B_x B_y^*$ (Table II). The phase difference $\angle B_z - \angle B_x$ was then determined by the preceding two. Noticeably, the phase difference values in Fig. 8 are mostly near 0 or π. This is expected from a linearly polarized RF vector field. Fig. 8(d-f) presents more quantitative comparison between the measurement and simulation. The relatively large errors in $\angle B_x - \angle B_y$ and $\angle B_z - \angle B_x$ (near $\pi/2$) compared to $\angle B_y - \angle B_z$ ($\sim \pi/10$) are due to noise sensitivity of $\angle B_x$ and are much suppressed when magnitude weighting is incorporated (normalized rms difference $<$ 13%, Fig. 8(e)). Despite visually satisfactory correlation of colors in Fig. 8(a-c), the correlation coefficients between the measured and simulated complex products ($B_x B_y^*$, $B_y B_z^*$, $B_z B_x^*$) were only moderate (Fig. 8(f)). This was because the spatial variation of these terms within each

2D measurement mask (where correlation was computed) was either weak ($B_y B_z^*$) or noisy ($B_x B_y^*$, $B_z B_x^*$). The correlation coefficient for $B_y B_z^*$ computed over all slices, for example, was 0.87, higher than in any one slice.

V. DISCUSSION

We have presented the first experimental demonstration of RF vector field mapping in MRI up to a common phase map. We proposed an eight-orientation solution to calculate the desired magnitude and phase maps from standard B_1^+ mapping data with minimal assumptions or prior information. We have also designed a special M-shaped phantom support frame to implement the proposed orientations for a loop coil without losing the coil's sensitivity in any orientation. Experimental results obtained from a volume coil and a loop coil generally agreed with simulation.

In this work RF simulation was used to validate the measured RF vector field components. Another validation that would not require simulation (and accompanying assumptions) could potentially be obtained by computing electrical properties from the measured RF fields through MREPT, and comparing them with the ground truth. Such validation will be particularly relevant in future development of the method, especially in conjunction with an alternative MREPT method as mentioned below.

A few remarks on the possibility of other multi-orientation solutions are in order. As explained in Supplementary materials (section 1), the six-orientation method of [16] yields the magnitudes $|B_x|$, $|B_y|$, $|B_z|$ and the sine of the relative phases $\angle B_x B_y^*$, $\angle B_y B_z^*$, $\angle B_z B_x^*$. If we call these phases α, β, γ, then a relevant question is: can one retrieve α and β from $\sin \alpha$, $\sin \beta$, and $\sin(\alpha + \beta)$ (since $\gamma = -\alpha - \beta$)? In many cases the four-fold ambiguity introduced by $\sin \alpha$ and $\sin \beta$ (that is, if (α, β) is a solution, so are $(\alpha, \pi - \beta)$, $(\pi - \alpha, \beta)$, $(\pi - \alpha, \pi - \beta)$) can be resolved by the knowledge of $\sin(\alpha + \beta)$. However, counterexamples exist where this is not the case, such as when $\alpha = 0$. In this case, the available information is reduced to $\sin \beta$ only, from which β cannot be uniquely determined within a 2π interval.

Another approach for alternative solutions is to focus on y-axis rotations only, which are more practical to implement. This is outlined in Supplementary materials, section 3. As with the case above, we find that y-axis rotations alone fail to provide full information to calculate the B_1 components including relative phases, regardless of the number and degrees of the rotation angles. Therefore, prior knowledge or other independent constraints would be needed for complete B_1 vector field determination. This may well be possible, and warrants further exploration in the future. We note that in any multi-orientation solution envisioned, the total scan time will be proportional to the number of orientations.

At the moment, the proposed eight-orientation method is only practical for objects and coils that are much smaller than the magnet's bore. In order to extend the method to human imaging, dramatic reduction of the rotation angles is necessary. Multi-orientation imaging of human head with small rotation angles has been shown to be feasible for
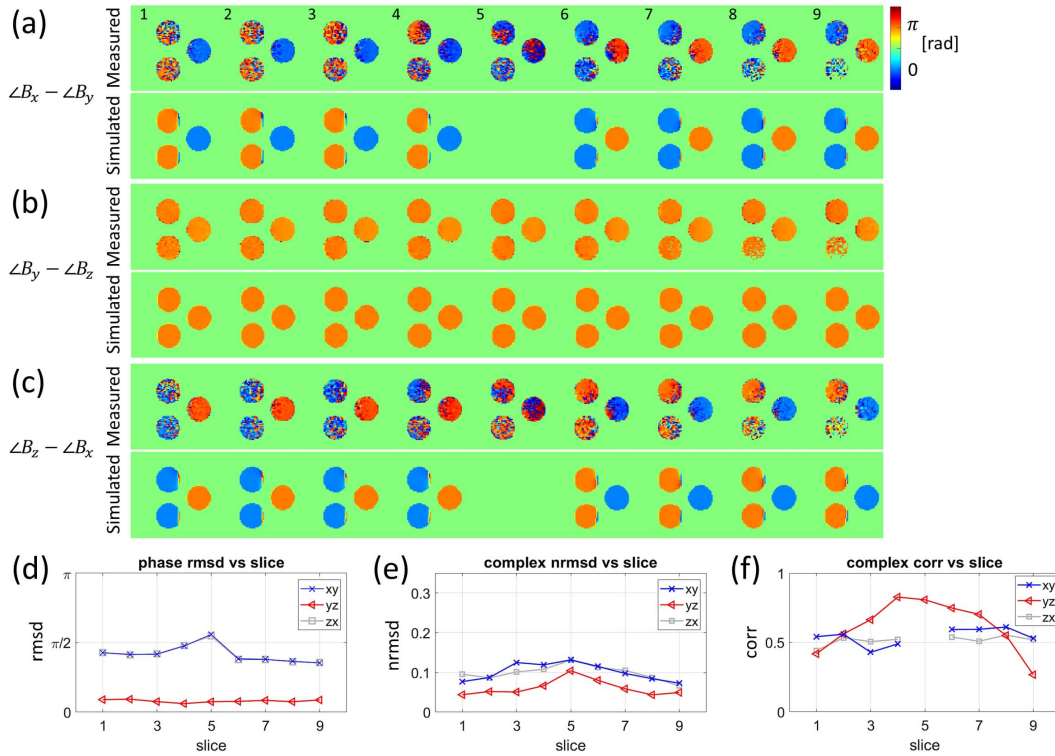
Fig. 8.   (a-c) Measured vs simulated relative phase maps between the $\vec{B}_1$ components in the phantom of Fig. 6. (d) Root-mean-square difference between the measured and simulated phases on each slice (calculated in the complex plane). (e-f) Magnitudes of the normalized rms difference (e) and the Pearson correlation coefficients (f) for the complex products ($B_x B_y^*$, $B_y B_z^*$, $B_z B_x^*$). The normalization in (e) was by the volume-averaged $\left| \vec{B}_1 \right|^2$.

quantitative susceptibility mapping [25] and susceptibility tensor imaging [26]. In our case, preliminary investigation indicated that small rotation angles (say within 45°) make the inverse problem of solving for B_1 components from the B_1^+ maps ill-conditioned. Such a problem might be satisfactorily handled with various regularization or machine learning techniques [27] to supplement available equations. For the latter, RF simulation with detailed human body model [28] could generate training data that link limited, measurable B_1 components with full RF vector solution. Instead of reducing angles in a conventional cylindrical magnet, it is also conceivable to implement large B_0-B_1 reorientation by rotating B_0 with a portable magnet. While much progress has been reported on portable MRI [29], such systems mostly employ Larmor frequencies at which RF propagation in biological tissue is less of an issue than in today's clinical systems.

Even for small objects as demonstrated in this work, our method has several limitations. First, our central hypothesis in deriving the theory (Eq. (3)) is that the RF field is effectively frozen in the object as the coil and the object arbitrarily reorient in the magnet bore. This can be violated if the RF field is not effectively decoupled from the surroundings, such as the RF shield in the magnet. The RF invariance is also compromised if the coil tuning is sensitive to the placement and twisting of RF cables which can happen in home-built coils. For the volume coil setup (which is larger than the loop coil), we performed a simulation to assess the effect of an

RF shield; we found up to 4% change in the RF field in the phantom due to the presence of a cylindrical RF shield of 68 cm diameter. Better isolation might be achieved by enclosing the object and the RF coil in their own RF shield that rotates along with them. In this case the RF field in the object will be altered by the additional shield but in a way that is independent of its orientation in the magnet.

Second, all B_1^+ mapping methods have a finite dynamic range, and many methods carry large uncertainties in measuring small flip angles, say below 20° [3]. In our method, the RF field in the object is projected onto the laboratory frame from many different angles, raising the possibility that some of them make flip angles too small to measure reliably. In our work we have carefully chosen the phantom and coil arrangement to minimize such flip angle voids. Our use of four different transmit voltages in the loop coil experiment was motivated by the dynamic range. However, the problem will worsen if the RF field in the object is strongly inhomogeneous. In follow-up studies we will investigate using phase-based B_1^+ mapping methods [30] that are known to provide relatively broad dynamic ranges.

Third, as the object changes orientation in the magnet, susceptibility-induced B_0 inhomogeneity in the object will also change [31], [32]. The effect will be more severe for non-spherical objects and in the presence of susceptibility-mismatched components such as metallic implants [33], [34]. Strong orientation-dependent static field changes can cause

difficulties in image registration via orientation-dependent pixel shifts and signal drop-outs. Use of large bandwidths and short echo times in image acquisition will mitigate the problem. In addition, the accuracy of B_1 mapping methods can be adversely affected by the Larmor frequency offset, with phase-based methods generally being more sensitive to off-resonance [2]. In some cases, encasing the entire object in a susceptibility-matched spherical housing can effectively reduce the orientation-dependent B_0 variation caused by air-water susceptibility boundaries [32]. Such a setup, however, can constrain RF coil placement near the object.

Any number of B_1^+ magnitude measurements cannot determine the absolute phase of the RF field. This can be seen from Eq. (3) by multiplying B_x, B_y, B_z by a common phase factor $e^{i\phi(\vec{r})}$, which will be factored out and reduced to unity. In order to do absolute phase measurement, one should measure quantities that involve B_1^+ phase. Several authors have demonstrated that by measuring B_1^+ phase relative to a receiver phase in a multiple transmitter system, absolute B_1^+ phase can be determined [5], [7], [35]. Such a method can naturally supplement the measurements described above to complete the absolute B_1 vector field mapping. A full, 3D complex RF magnetic field data could then enable deterministic calculation of the electrical properties [36] as well as the electric field. While noise amplification by differentiation will be an issue in such calculations, it will potentially mark a significant new development in biomedical RF field research with implications in RF safety and novel quantitative imaging.

VI. Conclusion

We have demonstrated that by conducting B_1^+ magnitude mapping at multiple orientations of the object and the RF coil with respect to the main magnetic field, one can calculate the magnitudes and relative phases of the three vector components of the RF magnetic field in the object. While not suitable for human applications, the proposed method could be used for validation of theories and simulations of RF heating and electrical properties measurements.

Appendix

Here we discuss the issue of obtaining the relative phase when one of the B_1 vector components is nearly zero. We are interested in the phase between the two non-zero components. Referring to Table II, if $B_y = 0$, the phase between B_z and B_x can be obtained from the real and imaginary parts of $B_z B_x^*$. Similarly, if $B_z = 0$, the phase between B_x and B_y is calculable from $Re\left(B_x B_y^*\right)$ and $Im\left(B_x B_y^*\right)$. On the other hand, if $B_x = 0$ then Table II allows determining $\angle B_y - \angle B_z$ only up to π's complement. That is, if θ is a solution, $\pi - \theta$ is too. This is because we have the magnitude $\left|B_y B_z^*\right| = \left|B_y\right|\left|B_z\right|$ and the imaginary part $Im\left(B_y B_z^*\right) = \left|B_y B_z^*\right| \sin\theta$ of the product $B_y B_z^*$, but not its real part from Table II. This two-fold degeneracy can possibly be lifted by prior information. In our loop coil case, the coil's orientation dictates that in the object's reference frame, the magnetic field vector in the central region of the coil should most likely be in the 2nd and the 4th quadrants of the yz plane. This means that B_y,

B_z phase difference should be close to π, not 0. That is, $Re\left(B_y B_z^*\right) < 0$, which allows unique determination of the complex $B_y B_z^*$ (and therefore its phase) by

$$B_y B_z^* = -\sqrt{\left|B_y B_z\right|^2 - Im\left(B_y B_z^*\right)^2} + i\,Im\left(B_y B_z^*\right).$$

Acknowledgment

References

[1] M. E. Ladd et al., "Pros and cons of ultra-high-field MRI/MRS for human application," Prog. Nucl. Magn. Reson. Spectrosc., vol. 109, pp. 1–50, Dec. 2018. [Online]. Available: https://www.sciencedirect.com/science/article/pii/S007965651830013X

[2] R. Pohmann and K. Scheffler, "A theoretical and experimental comparison of different techniques for B₁ mapping at very high fields," NMR Biomed., vol. 26, no. 3, pp. 265–275, Sep. 2012. [Online]. Available: https://onlinelibrary.wiley.com/doi/full/10.1002/nbm.2844

[3] G. R. Morrell and M. C. Schabel, "An analysis of the accuracy of magnetic resonance flip angle measurement methods," Phys. Med. Biol., vol. 55, no. 20, pp. 6157–6174, Sep. 2010. [Online]. Available: https://iopscience.iop.org/article/10.1088/0031-9155/55/20/008/pdf

[4] T. Voigt, H. Homann, U. Katscher, and O. Doessel, "Patient-individual local SAR determination: In vivo measurements and numerical validationn," Magn. Reson. Med., vol. 68, no. 4, pp. 1117–1126, 2012. [Online]. Available: https://onlinelibrary.wiley.com/doi/full/10.1002/mrm.23322

[5] S. Buchenau, M. Haas, D. N. Splitthoff, J. Hennig, and M. Zaitsev, "Iterative separation of transmit and receive phase contributions and B₁⁺-based estimation of the specific absorption rate for transmit arrays," Magn. Reson. Mater. Phys., Biol. Med., vol. 26, pp. 463–476, Feb. 2013. [Online]. Available: https://link.springer.com/article/10.1007/s10334-013-0367-6

[6] N. Boulant, U. Katscher, M. Luong, A. Massire, A. Amadon, and A. Vignaud, "B1+-based SAR assessment using a birdcage coil at 7 Tesla: Experimental evaluation using magnetic resonance thermometry," Presented at the 22nd Annu. Meeting ISMRM, May 2014. [Online]. Available: http://archive.ismrm.org/2014/4900.html

[7] U. Katscher, C. Findeklee, and T. Voigt, "B₁-based specific energy absorption rate determination for nonquadrature radiofrequency excitation," Magn. Reson. Med., vol. 68, no. 6, pp. 1911–1918, 2012. [Online]. Available: https://onlinelibrary.wiley.com/doi/full/10.1002/mrm.24215

[8] X. Zhang, J. Liu, and B. He, "Magnetic-Resonance-Based electrical properties tomography: A review," IEEE Rev. Biomed. Eng., vol. 7, pp. 87–96, 2014, doi: 10.1109/RBME.2013.2297206.

[9] Reporting of Computational Modeling Studies in Medical Device Submission-Guidance for Industry and FDA Staff, document FDA-2013-D-1530, Sep. 2016. [Online]. Available: http://www.fda.gov/downloads/MedicalDevices/DeviceRegulationandGuidance/GuidanceDocuments/UCM381813.pdf

[10] I. Hancu, J. Liu, Y. Hua, and S. Lee, "Electrical properties tomography: Available contrast and reconstruction capabilities," Magn. Reson. Med., vol. 81, no. 2, pp. 803–810, Feb. 2019. [Online]. Available: https://onlinelibrary.wiley.com/doi/full/10.1002/mrm.27453

[11] U. Katscher, D.-H. Kim, and J.-K. Seo, "Recent progress and future challenges in MR electric properties tomography," Comput. Math. Methods Med., vol. 2013, Mar. 2013, Art. no. 546562. [Online]. Available: https://www.hindawi.com/journals/cmmm/2013/546562/

[12] J. Liu, X. Zhang, S. Schmitter, P. F. Van de Moortele, and B. He, "Gradient-based electrical properties tomography (gEPT): A robust method for mapping electrical properties of biological tissues in vivo using magnetic resonance imaging," Magn. Reson. Med., vol. 74, pp. 634–646, Sep. 2015. [Online]. Available: https://onlinelibrary.wiley.com/doi/full/10.1002/mrm.25434

[13] E. Balidemaj et al., "CSI-EPT: A contrast source inversion approach for improved MRI-based electric properties tomography," IEEE Trans. Med. Imag., vol. 34, no. 9, pp. 1788–1796, Sep. 2015. [Online]. Available: https://ieeexplore.ieee.org/document/7046353/citations#citations

[14] N. Gurler and Y. Z. Ider, "Gradient-based electrical conductivity imaging using MR phase," *Magn. Reson. Med.*, vol. 77, no. 1, pp. 137–150, Jan. 2017. [Online]. Available: https://onlinelibrary.wiley.com/doi/full/10.1002/mrm.26097

[15] G. C. Scott, M. L. G. Joy, R. L. Armstrong, and R. M. Henkelman, "Electromagnetic considerations for RF current density imaging," *IEEE Trans. Med. Imag.*, vol. 14, no. 3, pp. 515–524, Sep. 1995. [Online]. Available: https://ieeexplore.ieee.org/document/414617

[16] F. Wiesinger, F. Seifert, H. Koenig, and K. P. Pruessmann, "Prospect of absolute B$_1$ calibration," Presented in session: Unsolved Problems Unmet Needs Magn. Reson., presented at the 14th Annu. Meeting ISMRM, May 2006. [Online]. Available: https://www.ismrm.org/06/UnsolvedProblems.htm

[17] S.-K. Lee and S. Oh, "B$_1$ vector field mapping through multi-orientation B1+ measurements," Presented at the 26th Annu. Meeting ISMRM, Jun. 2018. [Online]. Available: http://archive.ismrm.org/2018/4313.html

[18] W. R. Overall, J. M. Pauly, P. P. Stang, and G. C. Scott, "Ensuring safety of implanted devices under MRI using reversed RF polarization," *Magn. Reson. Med.*, vol. 64, no. 3, pp. 823–833, Sep. 2010. [Online]. Available: https://onlinelibrary.wiley.com/doi/full/10.1002/mrm.22468

[19] B.-P. Song, H.-S. Kim, K.-N. Kim, and S.-K. Lee, "Inductively coupled RF coil for imaging a 40 μm-thick histology sample in a clinical MRI scanner," *J. Korean Phys. Soc.*, vol. 77, pp. 87–93, Jul. 2020. [Online]. Available: https://link.springer.com/article/10.3938/jkps.77.87

[20] G. C. Scott, M. L. G. Joy, R. L. Armstrong, and R. M. Henkelman, "RF current density imaging in homogeneous media," *Magn. Reson. Med.*, vol. 28, no. 2, pp. 186–201, Dec. 1992. [Online]. Available: https://onlinelibrary.wiley.com/doi/abs/10.1002/mrm.1910280203

[21] J. Wang, M. Qiu, J. Watzl, R. de Graff, and R. T. Constable, "*In vivo* receive sensitivity measurement," Presented at the 17th Annu. Meeting ISMRM, Apr. 2009. [Online]. Available: http://archive.ismrm.org/2009/4564.html

[22] S. Belongie. *Rodrigues Rotation Formula From MathWorld-a Wolfram Web Resource*. Accessed: Dec. 8, 2020. [Online]. Available: http://mathworld.wolfram.com/RodriguesRotationFormula.html

[23] H.-P. Fautz, M. Vogel, P. Gross, A. Kerr, and Y. Zhu, "B1 mapping of coil arrays for parallel transmission," Presented at the 16th Annu. Meeting ISMRM, May 2008. [Online]. Available: https://cds.ismrm.org/ismrm-2008/files/01247.pdf

[24] G. H. Glover *et al.*, "Comparison of linear and circular polarization for magnetic resonance imaging," *J. Magn. Reson.*, vol. 64, no. 2, pp. 255–270, Sep. 1985. [Online]. Available: https://www.sciencedirect.com/science/article/pii/002223648590349X

[25] T. Liu *et al.*, "Morphology enabled dipole inversion (MEDI) from a single-angle acquisition: Comparison with COSMOS in human brain imaging," *Magn. Reson. Med.*, vol. 66, no. 3, pp. 777–783, Apr. 2011. [Online]. Available: https://onlinelibrary.wiley.com/doi/full/10.1002/mrm.22816

[26] X. Li and P. C. M. van Zijl, "Mean magnetic susceptibility regularized susceptibility tensor imaging (MMSR-STI) for estimating orientations of white matter fibers in human brain," *Magn. Reson. Med.*, vol. 72, no. 3, pp. 610–619, Jun. 2014. [Online]. Available: https://onlinelibrary.wiley.com/doi/full/10.1002/mrm.25322

[27] E. F. Meliado, "A deep learning method for image-based subject-specific local SAR assessment," *Magn. Reson. Med.*, vol. 83, no. 2, pp. 695–711, Feb. 2020. [Online]. Available: https://onlinelibrary.wiley.com/doi/full/10.1002/mrm.27948

[28] S. Gavazzi, "Deep learning-based reconstruction of *in vivo* pelvis conductivity with a 3D patch-based convolutional neural network trained on simulated MR data," *Magn. Reson. Med.*, vol. 84, no. 5, pp. 2772–2787, Nov. 2020. [Online]. Available: https://onlinelibrary.wiley.com/doi/full/10.1002/mrm.28285

[29] M. Mullen and M. Garwood, "Contemporary approaches to high-field magnetic resonance imaging with large field inhomogeneity," *Prog. Nucl. Magn. Reson. Spectrosc.*, vol. 120, pp. 95–108, Oct./Dec. 2020, doi: 10.1016/j.pnmrs.2020.07.003.

[30] L. I. Sacolick, F. Wiesinger, I. Hancu, and M. W. Vogel, "B$_1$ mapping by Bloch-Siegert shift," *Magn. Reason. Med.*, vol. 63, no. 5, pp. 1315–1322, Apr. 2010. [Online]. Available: https://onlinelibrary.wiley.com/doi/full/10.1002/mrm.22357

[31] S.-K. Lee, S.-H. Hwang, J.-S. Barg, and S.-J. Yeo, "Rapid, theoretically artifact–free calculation of static magnetic field induced by voxelated susceptibility distribution in an arbitrary volume of interest," *Magn. Reson. Med.*, vol. 80, no. 5, pp. 2109–2121, Nov. 2018. [Online]. Available: https://onlinelibrary.wiley.com/doi/full/10.1002/mrm.27161

[32] S.-H. Lee, M.-J. Han, J. Lee, and S.-K. Lee, "Experimental setup for bulk susceptibility effect-minimized, multi-orientation MRI of *ex vivo* tissue samples," *Med. Phys.*, vol. 47, no. 7, pp. 3032–3043, Jul. 2020, doi: 10.1002/mp.14174.

[33] J.-H. Kim, J.-H. Kim, S.-H. Lee, J. Park, and S.-K. Lee, "Fabrication of a spherical inclusion phantom for validation of magnetic resonance-based magnetic susceptibility imaging," *PLoS ONE*, vol. 14, no. 8, Aug. 2019, Art. no. e0220639, doi: 10.1002/mp.14174.

[34] X. Shi, E. Levine, H. Weber, and B. A. Hargreaves, "Accelerated imaging of metallic implants using model-based nonlinear reconstruction," *Magn. Reson. Med.*, vol. 81, no. 4, pp. 2247–2263, Apr. 2019. [Online]. Available: https://onlinelibrary.wiley.com/doi/full/10.1002/mrm.27536

[35] D. K. Sodickson, "Local Maxwell tomography using transmit-receive coil arrays for contact-free mapping of tissue electrical properties and determination of absolute RF phase," Presented at the 20th Annu. Meeting ISMRM, May 2012. [Online]. Available: http://archive.ismrm.org/2012/0387.html

[36] A. Nachman, D. Wang, W. Ma, and M. Joy, "A local formula for inhomogeneous complex conductivity as a function of the RF magnetic field," Presented in Unsolved problems and unmet needs in magnetic resonance: new standards, old mysteries, at the 15th Annual Meeting of ISMRM, May 2007. [Online]. Available: https://www.ismrm.org/07/Unsolved.htm